

PAPER • OPEN ACCESS

Large-area polycrystalline α -MoO₃ thin films for IR photonics

To cite this article: Maria Cristina Larciprete *et al* 2024 *J. Phys. D: Appl. Phys.* **57** 135107

View the [article online](#) for updates and enhancements.

You may also like

- [Role of Oxygen Vacancy Defects in the Electrochemical Performance of Substoichiometric Molybdenum Oxide](#)
Yanhua Cui, Kaiyuan Wei, Yu Zhao *et al.*
- [Sequential Deposition of Electrochromic MoO₃ Thin Films with High Coloration Efficiency and Stability](#)
Onur Turel, Serife O. Hacioglu, Sahin Coskun *et al.*
- [Effective degradation of Rhodamine B using \$\alpha\$ -MoO₃ nanoplates synthesised using thermal decomposition method](#)
Lakshmi Mohan, B Devu, Radhika R Menon *et al.*

PRIME
PACIFIC RIM MEETING
ON ELECTROCHEMICAL
AND SOLID STATE SCIENCE












HONOLULU, HI
Oct 6–11, 2024

Abstract submission deadline:
April 12, 2024

Learn more and submit!

Joint Meeting of
The Electrochemical Society
•
The Electrochemical Society of Japan
•
Korea Electrochemical Society

Large-area polycrystalline α -MoO₃ thin films for IR photonics

Maria Cristina Larciprete¹ , Daniele Ceneda¹ , Chiyu Yang² ,
Sina Abedini Dereshgi³ , Federico Vittorio Lupo⁴ , Maria Pia Casaletto⁵ ,
Roberto Macaluso⁴ , Mauro Antezza^{6,7} , Zhuomin M Zhang² , Marco Centini^{1,*} 
and Koray Aydin³ 

¹ Dipartimento di Scienze di Base ed Applicate per l'Ingegneria, Sapienza Università di Roma, Rome 00161, Italy

² George W. Woodruff School of Mechanical Engineering, Georgia Institute of Technology, Atlanta, GA 30332, United States of America

³ Department of Electrical and Computer Engineering, Northwestern University, Evanston, IL 60208, United States of America

⁴ Department of Engineering, University of Palermo, Palermo 90128, Italy

⁵ National Research Council (CNR), Institute for Nanostructured Materials (ISMN), Palermo 90146, Italy

⁶ Laboratoire Charles Coulomb (L2C), UMR 5221 CNRS-Université de Montpellier, F-34095 Montpellier, France

⁷ Institut Universitaire de France, 1 rue Descartes, F-75231 Paris Cedex 05, France

E-mail: marco.centini@uniroma1.it

Received 22 September 2023, revised 6 December 2023

Accepted for publication 20 December 2023

Published 5 January 2024



CrossMark

Abstract

In recent years, the excitation of surface phonon polaritons (SPhPs) in van der Waals materials received wide attention from the nanophotonics community. Alpha-phase Molybdenum trioxide (α -MoO₃), a naturally occurring biaxial hyperbolic crystal, emerged as a promising polaritonic material due to its ability to support SPhPs for three orthogonal directions at different wavelength bands (range 10–20 μ m). Here, we report on the fabrication, structural, morphological, and optical IR characterization of large-area (over 1 cm² size) α -MoO₃ polycrystalline film deposited on fused silica substrates by pulsed laser deposition. Due to the random grain distribution, the thin film does not display any optical anisotropy at normal incidence. However, the proposed fabrication method allows us to achieve a single α -phase, preserving the typical strong dispersion related to the phononic response of α -MoO₃ flakes. Remarkable spectral properties of interest for IR photonics applications are reported. For instance, a polarization-tunable reflection peak at 1006 cm⁻¹ with a dynamic range of $\Delta R = 0.3$ and a resonance Q -factor as high as 53 is observed at 45° angle of incidence. Additionally, we report the fulfillment of an impedance matching condition with the SiO₂ substrate leading to a polarization-independent almost perfect absorption condition ($R < 0.01$) at 972 cm⁻¹ which is maintained for a broad angle of incidence. In this framework our findings appear extremely promising for the further development of mid-IR lithography-free, scalable films, for efficient and large-scale sensors, filters, thermal emitters, and label-free biochemical sensing devices operating in the free space, using far-field detection setups.

* Author to whom any correspondence should be addressed.



Original content from this work may be used under the terms of the [Creative Commons Attribution 4.0 licence](https://creativecommons.org/licenses/by/4.0/). Any further distribution of this work must maintain attribution to the author(s) and the title of the work, journal citation and DOI.

Supplementary material for this article is available [online](#)

Keywords: optical phonons, vdW materials, polarization tuning, Reststrahlen band, hyperbolic materials, MoO₃

1. Introduction

Advances in nanophotonics have enabled the miniaturization of optical components due to the exploitation of surface plasmon polaritons (SPPs) [1] in the visible range that can strongly localize electromagnetic fields to small volumes. Recently, doped semiconductors [2, 3] and graphene [4] have been proposed to extend SPPs to the 2–8 μm range. Also, nanoantennas have been employed to achieve electric field localization in the mid-IR range for sensing applications. However, in order to take full advantage of surface-enhanced infrared absorption (SEIRA) techniques, a precise positioning of the analyte is required [5].

Moving toward the 8–20 μm wavelength range, where vibrational absorption peaks provide relevant information on molecular bonds, the SPP approach is less effective due to the poor field confinement at longer wavelengths [6]. Moreover, for the development of a complete IR photonic platform, miniaturization, and integration of optical components with the chip-scale platforms using facile fabrication techniques [7, 8] is highly desired. A conventional IR polarizer is nowadays designed using state-of-the-art holographic techniques [9] onto IR transparent support (CaF₂, ZnSe, BaF₂) with typical transmission losses of about 30%. Furthermore, the surface of such holographic grid polarizers is extremely delicate, and touching is absolutely to be avoided. Similarly, optical components such as polarization rotators have been realized using artificial metasurfaces [10] in the wavelength range up to 10 μm . Functionality at longer wavelengths is achieved using a combination of two parallel polarizers and by tilting the plates with respect to each other. Given the complexity of these components, their integration with the chip-scale platform can, therefore, be prohibitive and the challenge for an efficient, integrated and robust IR photonic platform persists.

Recent promising solutions are based on the exploitation of polar materials [11] including ultra-thin van der Waals (vdW) materials such as MoO₃, MoS₂, Ga₂O₃, hBN [12, 13]. Besides their strong anisotropy related to optical phonons (ideal for polarization rotation and control), they allow strong field localization by the excitation of surface waves called surface phonon polaritons (SPhPs), achieved through the coupling of the electromagnetic field with lattice vibrations. Several works reported on the great potential of polar materials for mid-IR sensing applications up to the terahertz (THz) regime [14, 15] and for the realization of compact IR photonic devices [16, 17].

Among vdW materials, Molybdenum trioxide (α -MoO₃) is attracting a great deal of attention [18] as it supports SPhPs in three different wavelength bands for the three orthogonal directions (range 10–20 μm), rendering this material a naturally

hyperbolic and biaxial material [19, 20]. Increased versatility can be obtained by combining it with other materials. Recent results show that α -MoO₃ can be combined with vanadium dioxide, (VO₂, a phase change material that undergoes insulator to metal phase transition at a temperature of 68 °C) [21, 22] in order to dynamically tune the polariton resonances. A metamaterial approach has also been proposed based on the random nanostructuring of α -MoO₃ with sub-wavelength dielectric elements (i.e. air ellipsoidal inclusions). This scheme could increase design versatility as well as tuning and hybridization of polariton modes [23]. Near- and far-field photonics effects have been theoretically explored integrating a α -MoO₃ film on a SiC metasurface on top of SiO₂ substrate showing interesting applications for surface polariton propagation control and radiative cooling [24].

Despite huge potential of this promising material, the development of a novel, highly versatile and compact α -MoO₃-based IR photonics platforms is hampered by the lack of availability of high-quality scalable films and/or multilayer stacks. α -MoO₃ for IR photonics and polaritonics is mostly used in the form of physical vapor deposition (PVD)-grown crystalline flakes. Although flakes allow exciting results in terms of hyperbolic phonon polariton excitation along x - and y -directions, there are several drawbacks that might limit the wide adaption of flakes geometries: the existing alignment techniques for flakes with a few tens of nanometers thickness are challenging; the flakes often have irregular shape preventing a good propagation of SPhPs; the dimensions of the flakes are usually limited to few hundreds of μm at most, therefore the large area or integrated/multifunctional devices are not practical. The fabrication process for obtaining such flakes is very complex, requiring investigation of strategies to create efficient conditions for films growth such as high temperatures (e.g. 780 °C [25]). Furthermore, a successive mechanical exfoliation process for transferring the desired MoO₃ 2D film onto a substrate of interest is needed [26]. In [27] a high confinement of near field signal corresponding to a Q factor of 40 has been reported in α -MoO₃ covering submicron-width trenches. These flakes are, however, difficult to handle and integrate in a practical device while keeping low fabrication costs. Moreover, they are relatively small for far-field applications since their dimensions often reach the diffraction limit of 10–20 μm range IR radiation thus requiring expensive and state of the art near-field detecting schemes.

The realization of single α -phase, oriented, large area MoO₃ film is still an open technological challenge. Atomic layer deposition (ALD), has been used to obtain good quality α -phase MoO₃ films, but only after 500 °C post-growth annealing [28]. This was necessary because deposition temperatures higher than 200 °C interfered with the stability

of the employed precursor. Furthermore, a long annealing time (>1 h) was required when the annealing was performed at lower temperatures than $500\text{ }^{\circ}\text{C}$. This means that, according to [29], ALD cannot be used to perform α -phase MoO_3 films deposition in one single step, making more difficult a possible integration of the MoO_3 film within a multilayer structure. ALD is, furthermore, an expensive tool employing hazardous precursors gases and even higher temperatures are needed for depositing MoO_3 by sublimation [30].

Conventional sputtering techniques were also employed to deposit MoO_3 films at room temperature. This led to a multi-phase crystalline MoO_3 film only after a post-growth annealing process [29–31]. When the annealing is performed at temperatures greater than $400\text{ }^{\circ}\text{C}$, it produces monoclinic β -phase MoO_3 films, not useful to exploit an optical phonons response [32]. Pulsed laser deposition (PLD) is a versatile and low-cost deposition technique which has already been employed for the deposition of α -phase MoO_3 films at $500\text{ }^{\circ}\text{C}$ [33] and other metal oxides such as VO_2 [34], and ZnO [35]. Compared with the exfoliation technique, it allows depositing large area MoO_3 films, which can be much more easily handled and integrated into a multilayer structure. However, to the best of our knowledge, a detailed IR characterization aimed at the identification of possible applications of the obtained films has not been reported so far for large area MoO_3 films deposited either by PLD or ALD. In the following, we show that PLD can be employed to obtain α - MoO_3 films at lower temperatures (e.g. $400\text{ }^{\circ}\text{C}$), without using harmful precursor gases normally employed by ALD and without the need of any post-growth annealing. Optical IR reflection spectra reveal a remarkable enhanced tunability of the reflection peak related to the z -axis phonon response as a function of the incident electric field polarization. Moreover, a polarization-independent perfect absorption condition is achieved for a broad angle of incidence. These features are not displayed from a single crystal flake. Our results show, for the first time, interesting possibilities for large-scale, lithography-free, polycrystalline MoO_3 film to be employed for IR signal management.

2. Sample fabrication

2.1. MoO_3 deposition

The mainly investigated structure in this study is composed of a 2200 nm (average thickness) MoO_3 film deposited on a fused silica substrate (figure 1(a)) using pulsed laser deposition at $400\text{ }^{\circ}\text{C}$ and 0.1 mbar of oxygen pressure. The PLD system employed uses a Q -switched tripled Nd:YAG laser (Quantel mod. YG78C20, $\lambda = 355\text{ nm}$) generating 6 ns width pulses with an energy of 80 mJ per pulse [33, 34, 36]. The density of energy was maintained at 1.2 J cm^{-2} , and the repetition rate was 4 Hz . The MoO_3 target was a 1 inch diameter, 0.25 inch -thick disk (purity 99.9%).

Before each deposition, the substrates were cleaned in an ultrasonic bath with acetone, subsequently rinsed with isopropanol and then dried with compressed air. After cleaning, each substrate was clamped onto an electrical heater, which allows achieving temperatures as high as $800\text{ }^{\circ}\text{C}$. The heater

was then placed inside a vacuum bell jar where oxygen gas can be introduced through an electromechanical valve to maintain the desired pressure.

The PLD deposition yields better crystallinity than sputtering due to its higher kinetic energy of ablated species. Furthermore, the PLD setup allows extremely versatile deposition conditions. Thus, the proper choice of deposition parameters and the resulting fabrication constraints is of crucial importance. In the present work, we focus attention on the best choice of parameters for the narrow band IR polarization filter functionality.

2.2. Structural and morphological characterization

X-ray diffraction (XRD) measurements were performed at room temperature to evaluate the crystalline structure of the deposited layers. XRD analysis was performed by using a D5005 diffractometer (Bruker AXS, Karlsruhe, Germany) equipped with a $\text{Cu K}\alpha$ (1.5406 \AA) source and operating at 40 kV and 30 mA . The following experimental conditions were used: 5 s acquisition time, 0.05° step in a 5° – 90° 2Θ angular range. XRD patterns showed that the high-quality MoO_3 films deposited at $400\text{ }^{\circ}\text{C}$ exhibited the stable orthorhombic α -phase of MoO_3 , as shown in figure 1(b). For the sake of completeness, we include in the supporting material the XRD pattern for a similar sample, deposited at a lower temperature (i.e., $200\text{ }^{\circ}\text{C}$), showing a monoclinic-only phase of the MoO_3 film (figure S1).

The surface morphology of the MoO_3 thin films has been characterized by using an Anfattech high speed atomic force microscope (AFM) as shown in figures 1(c) and (d), and Hitachi S-4700 cold field emission high-resolution scanning electron microscope (SEM) as shown in figure S2. Consistently with XRD measurements, the surface morphology captured by AFM and SEM images revealed a grain distribution in the thin film. The average grain size is around 400 nm and root-mean-square (RMS) roughness is about 100 nm . After the deposition, the film thickness was assessed by profilometry using a Dektak 150 profilometer. The average thickness was found to be approximately 2200 nm . Details on the profilometer measurements and a picture of the Sample are reported in figure S3 of the supporting material file.

3. Results and discussion

3.1. Polarization-dependent reflection measurements

IR reflection measurements have been performed using a FT-IR interferometer (Invenio-R, Bruker) in the spectral range 6000 – 400 cm^{-1} . The IR source was a glow-bar while the detector is based on deuterated triglycine sulfate (DTGS) pyroelectric detector. A total of 64 interferograms were acquired for each measurement, with a spectral resolution of 1 cm^{-1} . A sample area of $3 \times 3\text{ mm}^2$ was selected during IR data acquisition using knife-edge apertures. The FT-IR platform is equipped with a reflectance unit allowing to set the angles of incidence and reflectance, from almost normal incidence (about 13°) to grazing angles (85°) as illustrated

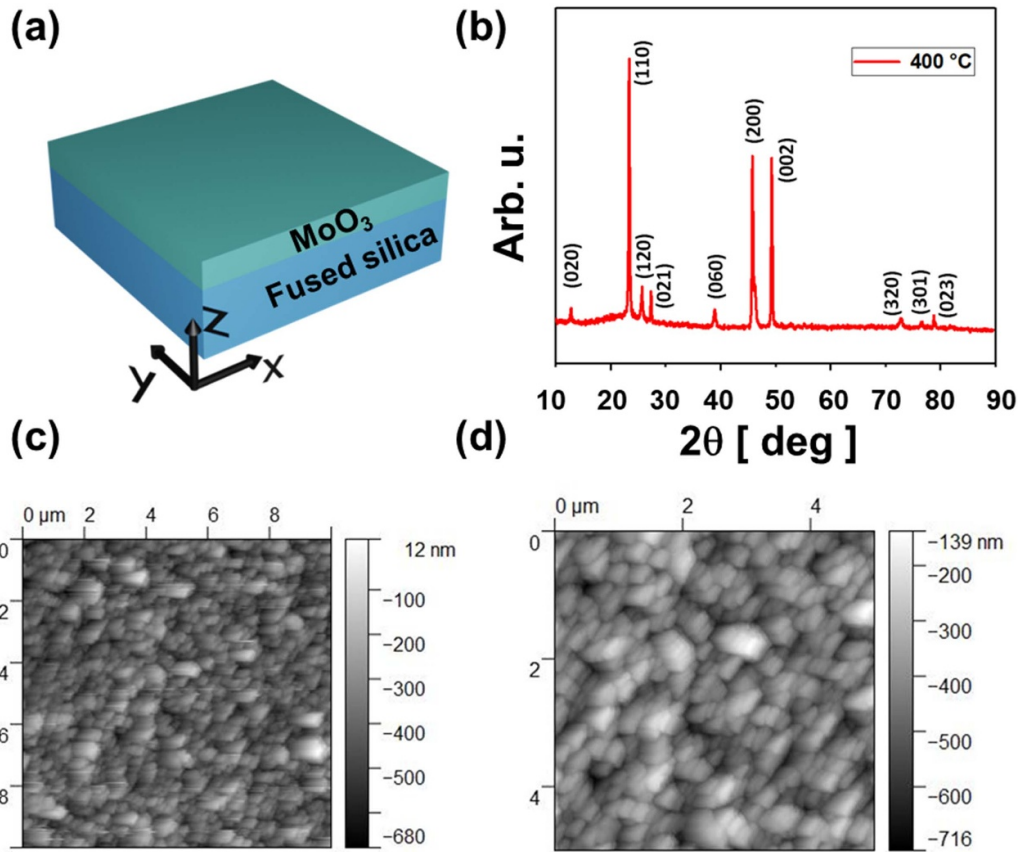


Figure 1. (a) Sketch of investigated sample. (b) X-ray diffraction (XRD) pattern of a MoO_3 film deposited onto fused silica by PLD at 400°C and 0.1 mbar oxygen pressure. The assigned peaks correspond to the orthorhombic phase of MoO_3 (ICDD 01-078-4612 card). (c), (d) AFM images of a MoO_3 film deposited onto fused silica by PLD: (c) image area $10 \times 10 \mu\text{m}^2$; (d) image area $5 \times 5 \mu\text{m}^2$.

in figure 2(a). The polarization state of incident light was selected using a holographic polarizing filter with a motorized mounter. Two different sets of measurements were performed with incidence angles of $\theta = 15^\circ$ and $\theta = 45^\circ$, respectively. Specifically, the reflectance spectra were recorded as a function of different linear polarization angles (ϕ) of the incoming light as sketched in figure 2(a). The measured spectral reflectance curves for different incidence angles and polarization of the incoming beam are shown in figures 2(b) and (c) for $\theta = 15^\circ$ and $\theta = 45^\circ$ incidence angles, respectively. Here $\phi = 0^\circ$ polarization angle stands for p-polarized light while $\phi = 90^\circ$ stands for s-polarized light. From figure (2(b)) we note that the polycrystalline nature of the laser-deposited MoO_3 simultaneously unveils, also at quasi normal incidence, the three Reststrahlen bands (RBs) associated to the alpha phase of bulk MoO_3 : the x -RB (edged by blue bars), corresponding to the frequency range from 820 cm^{-1} to 972 cm^{-1} ; the y -RB (red bars), extending at lower frequencies, between 545 cm^{-1} and 851 cm^{-1} and the z -RB (green bars), which is located between 962 cm^{-1} and 1010 cm^{-1} which is also partially overlapped with the RB of glass substrate (fused silica) from 1070 cm^{-1} to 1240 cm^{-1} [18]. We also note another RB of the glass substrate from 450 cm^{-1} to 505 cm^{-1} . Both glass RBs are delimited in figures 2(b) and (c) with black bars. Moreover, the polarization-resolved set of measurements, shows that at

quasi-normal incidence, the sample exhibits negligible in-plane anisotropy.

An ABB Bomen FTLA 2000FT-IR [37], was also used to measure the reflectance of the samples after 12 months of the sample growth. The results as presented in figure S4 agree very well with each other.

We focus our attention on the $900\text{--}1100 \text{ cm}^{-1}$ frequency range. We note that in this region interesting spectral features arise due to the overlap of two α - MoO_3 RBs and the near transverse optical phonon resonance of the glass substrate: (a) a perfect absorption condition at 972 cm^{-1} (measured reflectivity less than 1%); (b) a narrow band reflection peak at 1006 cm^{-1} . In order to extract more information on the behaviors of these features we also examined the reflection spectra at $\theta = 45^\circ$ incidence angle. Results are displayed in figure 2(c). We note that reflection spectra for polarizations angles $\phi = 45^\circ$ and $\phi = 135^\circ$ are nearly identical. This is another sign confirming that the MoO_3 film is polycrystalline and isotropic whereas the bulk MoO_3 would have displayed in-plane anisotropy. Nevertheless, we also note a big difference between reflectance for p-polarized ($\phi = 0^\circ$) and s-polarized ($\phi = 90^\circ$) incident fields. Indeed geometric out-of-plane anisotropy arises from the non-zero incidence condition. Figure 2(d) depicts a surface plot containing the experimental reflection spectra collected for different polarization angles ϕ ranging

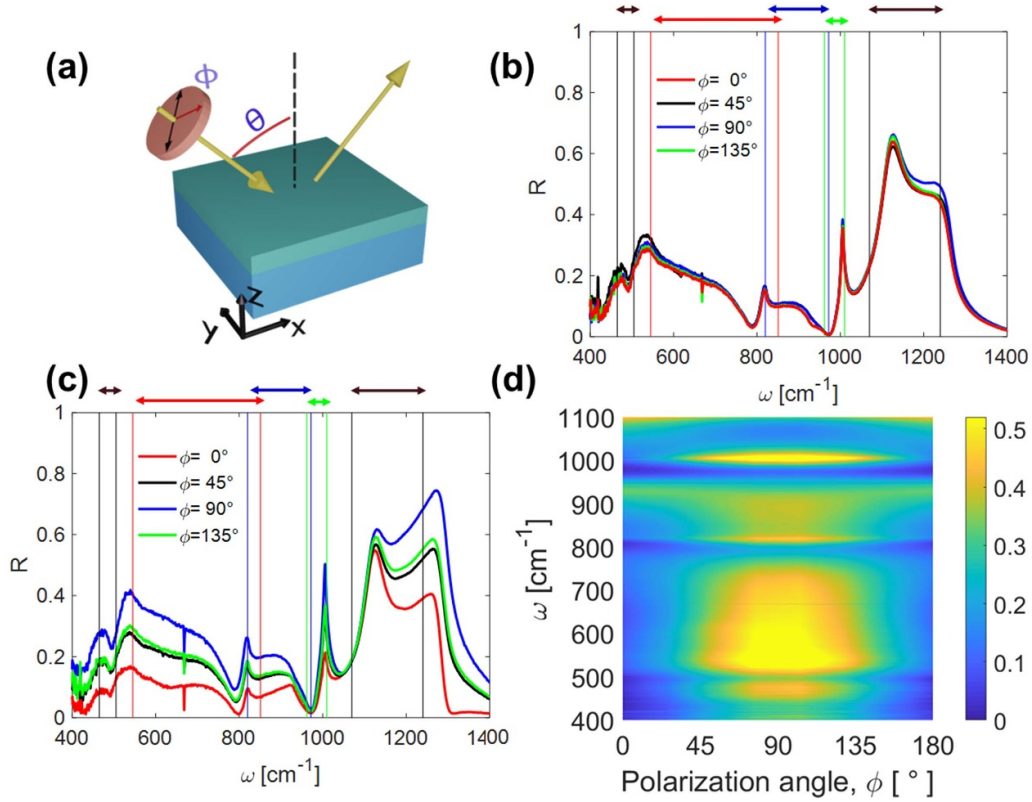


Figure 2. (a) Sketches of investigated experimental configuration: θ is the angle of incidence, ϕ is the polarization angle ($\phi = 0^\circ$ stands for p-pol and $\phi = 90^\circ$ stands for s-pol); polarization-dependent reflection FT-IR spectra measured at (b) $\theta = 15^\circ$ and (c) $\theta = 45^\circ$ incidence angle from a α -MoO₃ film, grown on fused silica substrate using pulsed laser deposition; As a reference we added the edges of the Reststrahlen bands of bulk α -MoO₃ along x - (blue), y - (red) and z - (green) directions. RBs of the glass substrate are depicted in black. (d) Surface plot of FT-IR reflection signal as a function of frequency and different polarization states of the incoming beam, measured at $\theta = 45^\circ$ incidence angle.

from 0° to 180° . The symmetry of the map with respect to $\phi = 90^\circ$ (s-polarization) is clear evidence that there is not in-plane anisotropy due to the polycrystalline nature of the MoO₃ film. Despite the geometrical anisotropy, we note that the perfect absorption condition at 972 cm^{-1} is almost preserved (minimum reflectivity ranges from 1% to 2%) for all polarization angles (note the almost horizontal low reflection line in figure 2(d)). Low reflection in this region is related to the fulfillment of an impedance-matching condition between air/ α -MoO₃/SiO₂. Although 972 cm^{-1} is slightly out of its RB, SiO₂ exhibits a non-negligible absorption at that frequency and the MoO₃ layer contributes minimizing the reflection losses thus maximizing the absorption. The low refractive index for MoO₃ around 972 cm^{-1} arises from the overlap between x - and z -RBs which affects the overall response of the polycrystalline film. The MoO₃ film acts as an antireflection coating at that frequency and the signal is efficiently absorbed by the SiO₂ substrate. Because of the low value of the refractive index at that frequency, the effect is preserved for a broad value of angle of incidence and it is not polarization-sensitive. In the next section, we will numerically verify the fulfillment of this condition.

A completely different scenario is presented at 1006 cm^{-1} . Indeed, for that frequency, a strong modulation of the MoO₃ film's infrared spectral features with the polarization of the

incoming light can be observed (figures 2(c) and (d)). Rotating the polarization state of incoming light (as highlighted in the legend) modifies both resonance intensity and width. It is worth noting that the polarization-dependent reflection peak at $\omega_{\text{max}} = 1006\text{ cm}^{-1}$ with a full width at half maximum (FWHM) $\Delta\omega = 17\text{ cm}^{-1}$ corresponding to a quality factor as high as $Q = \omega_{\text{max}}/\Delta\omega \sim 60$ is obtained in a lithography-free polar film. We note that the reflection peak is not a pure Lorentzian resonance. In order to provide a more accurate evaluation of the resonance linewidth we considered two Lorentzian-shaped curves respectively fitting the inner and the outer part of the experimental data. Results are reported in the supporting material (figure S5): the FWHM of the experimental resonance has been then retrieved by taking the average between the FWHMs of the Lorentzian curves and the maximum semi-dispersion as $\text{FWHM} \pm \Delta(\text{FWHM}) = (19 \pm 3)\text{ cm}^{-1}$. Thus the Q factor has been evaluated as $Q \pm \Delta Q = 53 \pm 8$. We finally include in the supporting material (figure S6) the reflection spectra of the previously mentioned monoclinic β -MoO₃ film (XRD pattern depicted in figure S1) for an incidence angle of 45° and several polarization angles. We note that the high- Q polarization-dependent reflection peak at 1006 cm^{-1} does not appear. Indeed this feature is specifically related to the α -MoO₃ optical phonon along the crystal z -axis (OPh_z) [18].

3.2. Theoretical models

Theoretical modeling of the optical properties of the polycrystalline α -MoO₃ film are performed considering the following observations. (1) The AFM images of surface morphology reported in figures 1(c) and (d) show that the grain sizes are much smaller than the infrared wavelengths in the measurements. (2) The almost negligible in-plane anisotropy demonstrated by the reflectance measurements at 15° angle of incidence (figure 2(b)) implies that the crystallite grains in the material are nearly randomly oriented. (3) The thickness of α -MoO₃ film varies from about 2000 nm to 2300 nm, as provided by the profilometer (see figure S3 of the supporting material file). Thus the material should be considered isotropic and homogenous, and an average thickness of 2200 nm is used in the simulation for this sample.

Conventional dispersion analysis of homogeneous composites seeks the effective dielectric function based on the individual constituents, also known as the effective medium theory (EMT) [38]. For example, polycrystal materials with various crystallite sizes can be predicted using a modified EMT proposed by Mayerhöfer [39, 40].

We also note that phonon frequencies in the polycrystalline sample can be shifted away from the TO and toward the LO position when compared with a perfect crystal. For instance, the resonance at 1006 cm⁻¹ in figures 2(b) and (c) is shifted with respect to the bulk α -MoO₃ $\omega_{z,TO} = 957$ cm⁻¹ [18]. This may be caused by the random orientation of crystallites in polycrystalline material, or the effect of air inclusions with an unknown volume fraction since a rough surface of α -MoO₃ film is observed. Due to such unknown parameters, EMT such as the Maxwell-Garnett theory or an arithmetic average of the principle dielectric functions did not provide a satisfactory agreement with the measured spectrum.

Therefore, an isotropic Lorentz model with three oscillators, which roughly correspond to the frequency values of the oscillators in the x -, y -, and z -directions of a perfect crystal α -MoO₃, is used to model the effective dispersion of the film:

$$\varepsilon(\omega) = \varepsilon_{\text{inf}} + \sum_{i=1}^3 \frac{S_i \omega_i^2}{\omega_i^2 - i\gamma_i \omega - \omega^2}; \quad (1)$$

The resonance frequencies ω_i , oscillator strengths S_i , damping coefficients γ_i in equation (1), with $i = 1, 2, 3$, and ε_{inf} , are determined as fitting parameters by minimizing the RMS deviation between the calculated and measured reflection spectra. The fused silica substrate is modeled using the optical constants from [41].

Initially, we used [42] to calculate the reflectance for anisotropic stratified media. However, since the α -MoO₃ film behaves as an isotropic medium we used the standard transfer matrix method for multilayer structures [38] in order to improve the speed and the efficiency of the fitting algorithm. Results obtained with the two methods are in perfect agreement. A thickness of 2200 nm is used in the calculation. The described fitting procedure applied to the experimental reflection spectra at 15° and 45° angle of incidences, allowed us to retrieve the parameters for the polycrystalline film with a

Table 1. Fitted Lorentz oscillator parameters for the polycrystalline α -MoO₃ film.

	S_i	ω_i (cm ⁻¹)	γ_i (cm ⁻¹)
1	1.224	560	151
2	0.100	841	33.0
3	0.023	1005	3.74
$\varepsilon_{\text{inf}} = 2.69$			

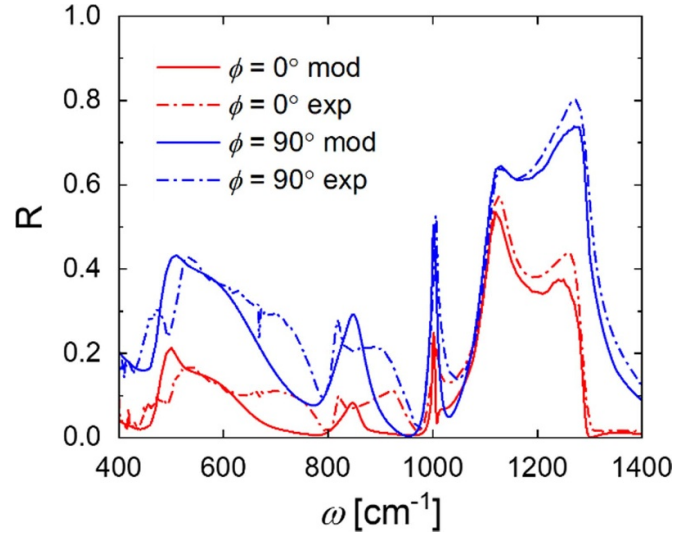


Figure 3. Comparison between the modeled (dash-dotted line) and the measured (solid line) reflectance spectra for s- and p-polarized incident fields at 45° angle of incidence.

RMS deviation of 0.054. The obtained parameters are listed in table 1 with a typical error bound of 20% considering uncertainties in the measurements and fitting.

As mentioned, there exist a shift of the phonon frequencies towards LO for the resonators when compared with the values for a perfect crystal α -MoO₃ reported in [18]: $\omega_{y,TO} = 545$ cm⁻¹, $\omega_{x,TO} = 821$ cm⁻¹ and $\omega_{z,TO} = 957$ cm⁻¹.

Figure 3 shows the comparison between the modeled and the measured reflectance spectra for s- and p-polarized incident fields at 45° angle of incidence. In figure 4 we compare the measured reflectance spectra at 15° of incidence with the theoretical predictions obtained with the fitted parameters evaluated from the previous data. In both cases, the model calculation is in reasonable agreement with the experiment, except for 600 cm⁻¹ < ω < 1000 cm⁻¹. A better agreement could be obtained if more oscillators were used. However, this was not done due to the lack of information, and it is not the focus of this work. Overall, the RMS deviation between the model and experiments is within 0.06 for the entire spectrum. Details on the modeling of different samples and the effect of thickness are reported in figures S7 and S8 of the supporting material, respectively. The previously discussed antireflection coating behavior at 972 cm⁻¹, can be verified by calculating the retrieved refractive index for the α -MoO₃ film and comparing it to the SiO₂ refractive index at the same frequency [41–43]. Our calculations show that the value of the refractive index of MoO₃ is extremely close (less than 2% relative difference)

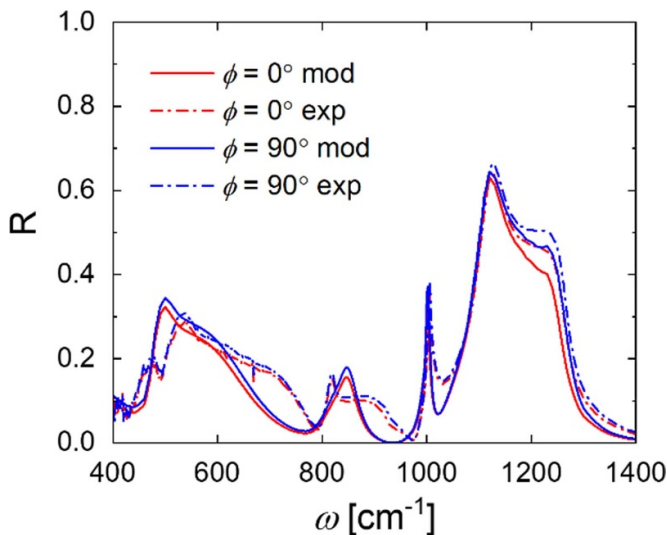


Figure 4. Comparison between the modeled (dash-dotted line) and the measured (solid line) reflectance spectra for s- and p-polarized incident fields at 15° angle of incidence.

to the square root of the refractive index of SiO_2 for that frequency. Moreover, the optical thickness of the MoO_3 film is close to a quarter wavelength stack. With fine optimization, it could behave as a perfect matching layer at that frequency.

As a final discussion, we focus on the small discrepancies between theoretical and experimental curves. It is worth mentioning that the reflectance measurement is performed with a measuring spot diameter of the order of a few millimeters. The inhomogeneity of the sampling area with varying surface roughness will result in the phonon frequency shifts to multiple positions. This effect leads to the deviation between experimental and theoretical data evaluated from a fixed frequency-oscillator model for calculation. This interpretation could also explain why the modeled spectra are less accurate for $\theta = 45^\circ$ angle of incidence with respect to $\theta = 15^\circ$. Indeed, at higher angles, the spot becomes larger, and sample inhomogeneity becomes more evident.

4. Conclusions

Flat optics requires the design of optical components into thin, planar, films to be integrated into photonic platforms. The use of vdW materials, leads to 2D flat optics with ultra-compact and tunable devices. Nevertheless, atomically thin optical elements suffer from alignment issues and will low possibilities of far-field applications. To overcome this limitation and achieve control and tuning of the spectral features over a large area, we prepared and investigated $\alpha\text{-MoO}_3$ films using pulsed laser deposition. Although deposition parameter optimization is still required for the definition of a process to synthesize MoO_3 films with a high degree of crystallinity, our experimental findings show remarkable spectral features

of the obtained polycrystalline films. Specifically, we reported both a polarization-independent perfect absorption behavior at 962 cm^{-1} well preserved for a broad angular incidence range, starting from normal incidence and an enhanced tunability vs. light polarization angle of a narrow band reflection peak at 1006 cm^{-1} with a Q factor of 53 ± 8 . The obtained high dynamic range of $\Delta R = 0.3$ with off-normal-excitation (which can be improved with increased incidence angle, see figure S9 in supporting material) is reliable and repeatable and results in wide tunability that may have great potential for label-free biochemical sensing application and narrow-band detection in the IR range without the use of time- and cost-consuming lithographic processes. In particular, the investigated sharp resonance can find applications to identify a spectral marker associated with specific moieties such as phenylalanine [44] tryptophan [45] to give some examples. We stress the point that the low fabrication cost and the Q -factor are not the only two relevant parameters to take into account. The possibility to operate with large sensing area without the need for microscopy or near-field techniques is an important benefit. Our large-area samples only require a basic far-field source/detector scheme, making them suitable for low-cost, mass distribution devices.

Data availability statement

All data that support the findings of this study are included within the article (and any supplementary files).

Acknowledgments

K A acknowledges support from the Air Force Office of Scientific Research under Award Number FA9550-22-1-0300. K A and M C L also acknowledge the support from University La Sapienza for the Visiting Professor Program 2020 (Bando Professori Visitatori 2020). M C, M C L, M A and Z M Z acknowledge the KITP program ‘Emerging Regimes and Implications of Quantum and Thermal Fluctuational Electrodynamics’ 2022, where part of this work has been done. This research was supported in part by the National Science Foundation under Grant No. PHY-1748958. C Y was supported by the National Science Foundation (CBET-2029892).

ORCID iDs

Maria Cristina Larciprete  <https://orcid.org/0000-0002-7876-628X>
 Daniele Ceneda  <https://orcid.org/0009-0002-4893-6310>
 Chiyu Yang  <https://orcid.org/0000-0002-5204-3622>
 Sina Abedini Dereshgi  <https://orcid.org/0000-0003-2929-0817>
 Federico Vittorio Lupo  <https://orcid.org/0000-0001-5761-698X>
 Maria Pia Casaletto  <https://orcid.org/0000-0002-2236-5671>
 Roberto Macaluso  <https://orcid.org/0000-0002-7612-3192>

Mauro Antezza  <https://orcid.org/0000-0003-4540-5864>
 Zhuomin M Zhang  <https://orcid.org/0000-0002-6774-6806>

Marco Centini  <https://orcid.org/0000-0003-0625-0054>
 Koray Aydin  <https://orcid.org/0000-0002-3268-2216>

References

- [1] Maier S A 2007 *Plasmonics: Fundamentals and Applications* (Springer)
- [2] Taliercio T and Biagioni P 2019 *Nanophotonics* **8** 949990
- [3] Martínez J, Ródenas A, Aguiló M, Fernández T, Solís J and Díaz F 2016 *Opt. Lett.* **41** 2493
- [4] Rodrigo D, Limaj O, Janner D, Etezadi D, Garcia De Abajo F J, Pruneri V and Altug H 2015 *Science* **349** 165168
- [5] De Ninno A, Ciasca G, Gerardino A, Calandrini E, Papi M, De Spirito M, Nucara A, Ortolani M, Businaro L and Baldassarre L 2015 *Phys. Chem. Chem. Phys.* **17** 21337–42
- [6] Occhicone A et al 2021 *ACS Photonics* **8** 350–9
- [7] Law S, Podolskiy V and Wasserman D 2013 *Nanophotonics* **2** 103–30
- [8] Fang Y, Ge Y, Wang C and Zhang H 2019 *Laser Photon. Rev.* **14** 1900098
- [9] Xia J, Yuan Z, Wang C, He C, Guo J and Wang C 2019 *OSA Contin.* **2** 1683–92
- [10] Wu Z, Ra'di Y and Grbic A 2019 *Phys. Rev. X* **9** 011036
- [11] Chen Y et al 2014 *ACS Photonics* **1** 718–24
- [12] Tamagnone M, Ambrosio A, Chaudhary K, Jauregui L A, Kim P, Wilson W L and Capasso F 2018 *Sci. Adv.* **4** eaat7189
- [13] Basov D N, Fogler M M and Garcia de Abajo F J 2016 *Science* **354** 6309
- [14] Caldwell J D, Lindsay L, Giannini V, Vurgaftman I, Reinecke T L, Maier S A and Glembocki O J 2015 *Nanophotonics* **4** 44–68
- [15] Folland T G, Lu G, Bruncz A, Nolen J R, Tadjer M and Caldwell J D 2020 *ACS Photonics* **7** 614621
- [16] Abedini Dereshgi S, Folland T G, Murthy A A, Song X, Tanriover I, Dravid V P, Caldwell J D and Aydin K 2020 *Nat. Commun.* **11** 5771
- [17] Álvarez-Pérez G, González-Morán A, Capote-Robayna N, Voronin K V, Duan J, Volkov V S, Alonso-González P and Nikitin A Y 2022 *ACS Photonics* **9** 383–90
- [18] Álvarez-Pérez G et al 2020 *Adv. Mater.* **32** 1908176
- [19] Chen M, Lin X, Dinh T H, Zheng Z, Shen J, Ma Q, Chen H, Jarillo-Herrero P and Dai S 2020 *Nat. Mater.* **19** 1307–11
- [20] Zheng Z et al 2019 *Sci. Adv.* **5** eaav8690
- [21] Larciprete M C, Centini M, Paoloni S, Fratoddi I, Abedini Dereshgi S, Tang K, Wu J and Aydin K 2020 *Sci. Rep.* **10** 11544
- [22] Abedini Dereshgi S, Larciprete M C, Centini M, Murthy A A, Tang K, Wu J, Dravid V P and Aydin K 2021 *ACS Appl. Mater. Interfaces* **13** 48981–7
- [23] Larciprete M C, Abedini Dereshgi S, Centini M and Aydin K 2022 *Opt. Express* **30** 12788–96
- [24] Erçağlar V, Hajian H, Rukhlenko I D and Ozbay E 2022 *Appl. Phys. Lett.* **121** 182201
- [25] Zheng Z et al 2018 *Adv. Mater.* **30** 1705318
- [26] Wei C, Abedini Dereshgi S, Song X, Murthy A, Dravid V P, Cao T and Aydin K 2020 *Adv. Opt. Mater.* **8** 2000088
- [27] Yang J, Tang J, Ghasemian M B, Mayyas M, Yu Q V, Li L H and Kalantar-Zadeh K 2022 *ACS Photonics* **9** 905–13
- [28] Fjellvåg Ø S, Ruud A, Sønsteby H H, Nilsen O and Fjellvåg H 2020 *Cryst. Growth Des.* **20** 3861–6
- [29] Ahmadpour M et al 2019 *ACS Appl. Energy Mater.* **2** 420–7
- [30] Atuchin V V, Gavrilova T, Grigorieva T I, Kuratieva N, Okotrub K, Pervukhina N V and Surovtsev N V 2011 *J. Cryst. Growth* **318** 987–90
- [31] Pérez-González M, Morales-Luna M, Santoyo-Salazar J, Crotte-Ledesma H, García-Tinoco P E and Tomás S A 2021 *Catal. Today* **360** 138–46
- [32] Park W-H, Lee G-N and Kim J 2018 *Sens. Actuators A* **271** 251–6
- [33] Holovský J, Horynová E, Horák L, Ridzoňová K, Remeš Z, Landová L and Kumar Sharma R 2021 *Vacuum* **194** 110613
- [34] Cesca T, Scian C, Petronijevic E, Leahu G, Li Voti R, Cesarini G, Macaluso R, Mosca M, Sibilia C and Mattei G 2020 *Nanoscale* **12** 851
- [35] Mosca M, Macaluso R, Cali C, Butté R, Nicolay S, Feltn E, Martin D and Grandjean N 2013 *Thin Solid Films* **539** 55
- [36] Boughelout A, Macaluso R, Crupi I, Megna B, Aida M S and Kechouane M 2019 *J. Electron. Mater.* **48** 4381
- [37] Wang L P, Lee B J, Wang X J and Zhang Z M Spatial and temporal coherence of thermal radiation in asymmetric Fabry–Perot resonance cavities *Int. J. Heat Mass Transfer* **52** 3024–31
- [38] Zhang Z M 2020 *Nano/Microscale Heat Transfer* 2nd edn (Springer)
- [39] Mayerhöfer T G 2002 *Appl. Spectrosc.* **56** 1194–205
- [40] Mayerhöfer T G 2004 *Vib. Spectrosc.* **35** 67–76
- [41] Palik E D 1998 *Handbook of Optical Constants of Solids* (Academic)
- [42] Passler N C and Paarmann A 2017 *J. Opt. Soc. Am. B* **34** 2128–39
- [43] Kitamura R, Pilon L and Jonasz M 2007 *Appl. Opt.* **46** 8118–33
- [44] Mahalakshmi R, Linet J M, Priya S N, Boaz B M, Jesuraja S X and Jerome Das S 2006 *Cryst. Res. Technol.* **41** 1072–5
- [45] Asher S A, Ludwig M and Johnson C R 1986 *J. Am. Chem. Soc.* **108** 3186–97